

See discussions, stats, and author profiles for this publication at: <https://www.researchgate.net/publication/265728935>

Synthesis and Ultrafast Carrier Dynamics of Single-Crystal Two-Dimensional CuInSe₂ Nanosheets

ARTICLE in JOURNAL OF PHYSICAL CHEMISTRY LETTERS · AUGUST 2014

Impact Factor: 7.46

READS

49

1 AUTHOR:



Xin Tao

Washington State University

8 PUBLICATIONS 24 CITATIONS

SEE PROFILE

Synthesis and Ultrafast Carrier Dynamics of Single-Crystal Two-Dimensional CuInSe₂ Nanosheets

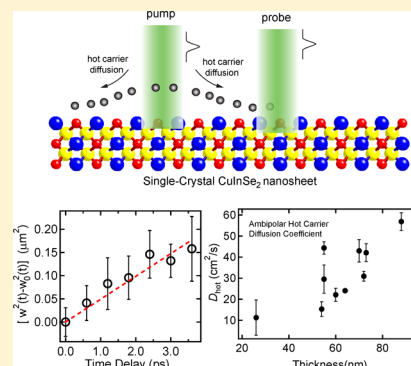
Xin Tao, Elham Mafi, and Yi Gu*

Department of Physics and Astronomy, Washington State University, Pullman, Washington 99164, United States

Supporting Information

ABSTRACT: We report, for the first time, the synthesis of single-crystal two-dimensional (2D) CuInSe₂ nanosheets and the studies of ultrafast carrier dynamics and transport in this 2D material. Particularly, single-crystal 2D CuInSe₂ with various thicknesses in the nanometer regime were fabricated by a solid-state chemical reaction between Cu and single-crystal exfoliated In₂Se₃ nanosheets. Characteristics of transient optical reflectivity, obtained from femtosecond optical pump–probe measurements on single CuInSe₂ nanosheets, suggest that the hot carrier cooling process dominates the carrier dynamics within a few picoseconds following the optical excitation. Spatially resolved pump–probe measurements, coupled to simple model calculations, were used to obtain the ambipolar hot carrier diffusion coefficient in single nanosheets. The dependence of the hot carrier diffusion coefficient on the nanosheet thickness provides insight into the limiting mechanisms of hot carrier transport and can be used to gauge the possibility of efficient hot carrier collection in nanostructured CuInSe₂ solar cells.

SECTION: Physical Processes in Nanomaterials and Nanostructures



The dynamics and transport of hot carriers in semiconductors provide insight into fundamental processes such as carrier–phonon and carrier–carrier interactions and also play an important role in many devices, including tunnel transistors¹ and quantum-cascade lasers.² In addition, high-efficiency solar cells that collect photogenerated hot carriers were also proposed and are being extensively studied.^{3–8} Recently, two-dimensional (2D) materials have received significant interest for photovoltaic applications, in light of efficient photon–electron conversions (e.g., in graphene),⁹ the recent discoveries of strong optical absorptions (e.g., in MoS₂ and WS₂),^{10,11} and the inherently low series resistance that minimizes the internal energy loss. A understanding of hot carrier dynamics and transport properties will further their potential for efficient photovoltaics.

Many advantages of these materials originate from the 2D geometry. One example is the excitonic effects due to the decreased dielectric screening in 2D, which contributes significantly to the enhanced optical absorptions.¹² This motivates the explorations of other more “conventional” semiconductors in the 2D form for solar cell applications. One material of interest is CuInSe₂, with CuInSe₂-based solar cells among the most efficient thin-film technologies.^{13,14} CuInSe₂ nanostructures, including nanocrystals^{15–20} and nanowires,^{21,22} have been synthesized, and the photovoltaic performance is being studied. However, the synthesis and the properties of 2D CuInSe₂ remain unexplored (to the best of our knowledge).

Here, we report, for the first time, the synthesis of single-crystal CuInSe₂ nanosheets with the thickness on the

nanometer scale and the studies of ultrafast carrier dynamics in this 2D material. Specifically, single-crystal CuInSe₂ nanosheets with various thicknesses were fabricated by a solid-state chemical reaction between Cu and single-crystal exfoliated In₂Se₃ nanosheets. Carrier dynamics in single nanosheets was studied via the measurements of the transient optical reflectivity using a femtosecond optical pump–probe technique. Hot carrier cooling was suggested to dominate the carrier dynamics within a few picoseconds following the optical excitation. The ambipolar hot carrier diffusion coefficient was obtained by spatially resolved pump–probe measurements on single nanosheets. The dependence of the hot carrier diffusion coefficient on the nanosheet thickness provides insight into the limiting mechanisms of hot carrier transport and can be used to gauge the possibility of efficient hot carrier collection in nanostructured CuInSe₂ solar cells.

The procedures for synthesizing 2D CuInSe₂ nanosheets are shown schematically in Figure 1a. First, 2D In₂Se₃ nanosheets with various thicknesses were mechanically exfoliated from α -phase In₂Se₃ powders (Alfa Aesar, 99.99%) onto SiO₂/Si and SiN/Si substrates.²³ The single-crystal nature and the (001) orientation of these nanosheets were verified by our recent work²³ and that of others.²⁴ Next, Cu was deposited via sputtering, followed by annealing under a flow of high-purity Ar at 350 °C for 1–1.5 h. The annealing leads to a solid-state reaction between Cu and In₂Se₃, which has been used to obtain

Received: June 17, 2014

Accepted: August 1, 2014

Published: August 6, 2014

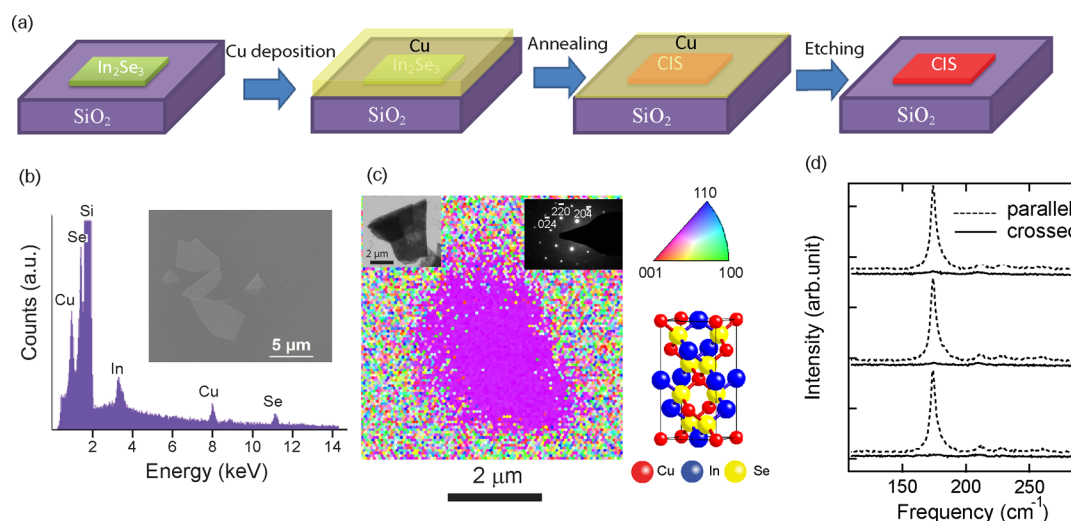


Figure 1. (a) Schematic procedures for synthesizing 2D CuInSe₂ nanosheets; (b) an EDX spectrum of a typical CuInSe₂ nanosheet, with a SEM image of several nanosheets shown in the inset; (c) an EBSD inverse pole orientation map of a typical CuInSe₂ nanosheet, with the inverse pole figure color scheme and the schematic chalcopyrite CuInSe₂ structure shown on the right and the inset showing a typical transmission electron microscopy image and a diffraction pattern of CuInSe₂ nanosheets; (d) polarized Raman spectra on a single CuInSe₂ nanosheet measured from multiple locations, with the dashed (solid) lines representing the parallel (crossed) configuration of excitation and detection polarizations.

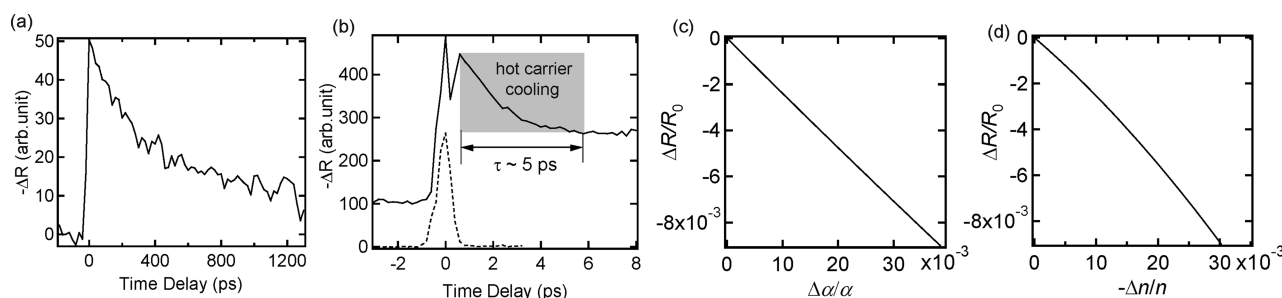


Figure 2. (a) Transient reflection signal ($-\Delta R$) from a single CuInSe₂ nanosheet; (b) $-\Delta R$ (solid line) close to the time zero, with the dashed line representing the autocorrelation signal obtained on a blank SiO₂/Si substrate; calculated $\Delta R/R_0$ as a function of (c) $\Delta\alpha/\alpha$ and (d) $-\Delta n/n$.

single-crystal CuInSe₂ nanowires.^{21,25} The excess Cu was then etched away by submerging the samples in 3 M aqueous HCl for 1 h and then rinsing with DI water. For the ultrafast optical pump–probe reflectivity measurements, emissions from a Yb/glass laser, which have a central wavelength at 517 nm with the pulse duration of ~ 200 fs and a repetition frequency of 20 MHz, were split into pump and probe pulses with the time delay provided by a linear translation stage. The typical pump fluence is $\sim 100\text{--}300$ $\mu\text{J}/\text{cm}^2$. These pulses are mechanically chopped at different frequencies and focused onto single CuInSe₂ nanosheets via a microscope objective. The reflected probe pulses, which were detected by a Si photodetector at the frequency equal to the sum of the pump and probe modulation frequencies using a lock-in amplifier, represents the differential reflection signal, ΔR . Further details can be found in ref 26.

A typical scanning electron microscope (SEM) image of several CuInSe₂ nanosheets is shown in the inset to Figure 1b. The stoichiometry of these nanosheets was obtained by energy-dispersive X-ray spectroscopy (EDX); an example of the EDX spectrum is shown in Figure 1b, with the Si peak presumably from the SiN/Si substrate. The average Cu/In/Se atomic ratio from several nanosheets is 1.0:0.8:1.9, in reasonable agreement with stoichiometric CuInSe₂. The single-crystal nature of the CuInSe₂ nanosheets is verified by electron backscatter diffraction (EBSD) mapping (Figure 1c), which shows predominantly a (112)-chalcopyrite (CH)-CuInSe₂ orienta-

tion. Such an orientation is consistent with the results from single-crystal CuInSe₂ nanowires obtained using a similar procedure.²⁷ A typical transmission microscopy (TEM) image is shown in the inset to Figure 1c. An example of the TEM diffraction pattern, also shown in the inset to Figure 1c, is consistent with the single-crystal nature and the (112)-CuInSe₂ orientation. To further confirm the single crystallinity, we also performed polarized Raman spectroscopy on single CuInSe₂ nanosheets using a Renishaw InVia Raman microscope with a 632 nm laser excitation. The polarized Raman spectra are sensitive to the symmetry of the zone-center phonons and therefore can be used to determine the crystal orientation. As shown in Figure 1d, under the parallel-polarization condition (the same linear polarization directions for excitation and detection), a strong A₁ lattice phonon mode of the CH-CuInSe₂ at ~ 174 cm^{-1} is observed,²⁸ with two additional small peaks at 212 and 230 cm^{-1} from the B₂ and E modes in CH-CuInSe₂.²⁹ The A₁ mode becomes very weak under the cross-polarization condition (perpendicular linear polarization directions for excitation and detection). This change in the A₁ mode intensity is consistent with previous polarized Raman studies on (112)-oriented CuInSe₂ single crystals.³⁰ Most importantly, polarized Raman spectra measured from multiple locations on single CuInSe₂ nanosheets, as shown in Figure 1d, exhibit the same characteristics, further confirming the single-crystal orientation of these nanosheets.

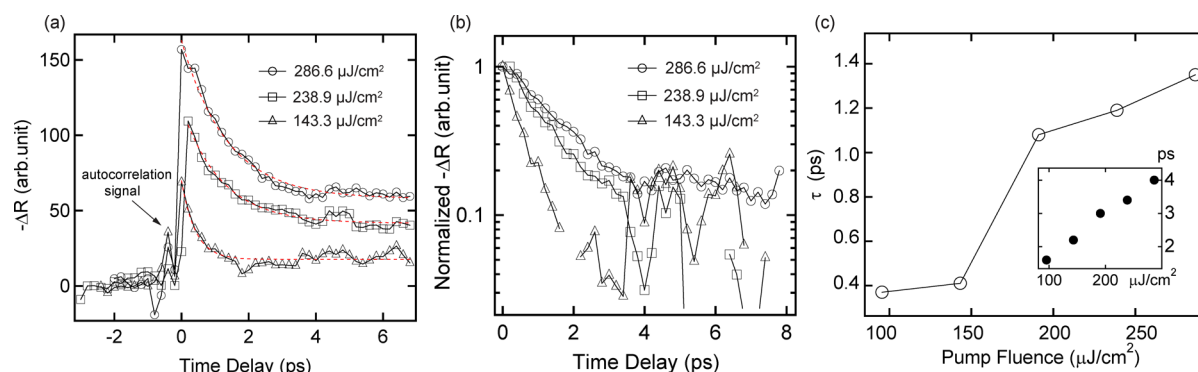


Figure 3. (a) $-\Delta R$ (solid lines) under various pump fluences fitted by single exponentials (dashed lines); (b) semilogarithmic plot of normalized $-\Delta R$ with the background (due to much slower decays at later time delays) subtracted; (c) the characteristic decay time, τ (open circles), extracted from the exponential fittings, with the time intervals (solid circles) for the entire hot carrier cooling process plotted in the set, as a function of the pump fluence.

The single crystallinity of CuInSe_2 nanosheets allows for the studies of intrinsic carrier dynamics without the contributions from grain boundaries. Figure 2a shows the transient differential reflectivity, $-\Delta R$, from a single CuInSe_2 nanosheet as a function of probe delay, with the delay time extending beyond 1 ns. We note that ΔR is negative. The typical maximum ratio between ΔR and R_0 (reflectivity without the pump pulses) is on the order of 10^{-3} . A closer look at the decay of $-\Delta R$ around the time zero, as shown in Figure 2b, reveals an initial sharp rise, which we attribute to the nonlinear process in the Si photodetector, and is thus not related to the sample response. This is confirmed by the autocorrelation scan (dashed line in Figure 2b) performed on a blank SiO_2/Si substrate, with a full width at half-maximum (fwhm) of ~ 0.6 ps. After the sharp rise, $-\Delta R$ decays rapidly in the first few picoseconds followed by a much slower decrease that corresponds to the slow decay in Figure 2a. This slow decay, with more details provided in the Supporting Information, can be attributed to combined effects of Auger recombination and trap-assisted processes, which are on the order of nanoseconds in CuInSe_2 .³¹ In the following, we focus on the fast initial decay of ΔR by first considering the origin of the negative ΔR , followed by a discussion of the possible mechanisms for the fast initial decay of ΔR .

ΔR originates from the pump-induced changes in the complex refractive index, $\eta = n - i(\alpha\lambda/4\pi)$, where n , α , and λ are the real refractive index, absorption coefficient, and the light wavelength, respectively. As the direct band gap of CuInSe_2 is ~ 1.02 eV (see also the Supporting Information for absorption measurements), the pump pulses with the energy of ~ 2.4 eV generate excess carriers (electrons and holes) that can lead to changes in both n and α . By considering a model of multiple reflections from CuInSe_2 , SiO_2 , and Si interfaces (see the Supporting Information),³² we calculated $\Delta R/R_0$ as a function of $\Delta\alpha/\alpha$ and $\Delta n/n$. As shown in Figure 2c and d, a negative $\Delta R/R_0$ indicates an increase in the absorption coefficient (positive $\Delta\alpha$) and/or a decrease in the real refractive index (negative Δn). We note that $\Delta\alpha$ and Δn are related to each other via the Kramers–Kronig relation.

The major mechanisms that can contribute to $\Delta\alpha$ and Δn in semiconductors include band gap renormalization, band filling, and free-carrier absorption.^{33,34} The band gap renormalization (i.e., the band gap shrinkage) originates from the correlation effect of carriers, which becomes significant when the generated carrier density is high. A critical carrier density³³ can be

estimated for CuInSe_2 to be $\sim 10^{18} \text{ cm}^{-3}$. Given the rather high pump fluences used in this study, which correspond to excess carrier densities of $\sim 10^{19}–10^{20} \text{ cm}^{-3}$, the band gap renormalization is expected to be significant in our case. This effect always leads to a positive $\Delta\alpha$ and, according to the Kramers–Kronig relation, to a negative Δn when the pump–probe pulse energies are above the band gap.^{33,34} This contributes to a negative ΔR , as observed. On the other hand, the band filling effect, where α decreases due to the occupation of the band states by generated carriers, leads to a negative $\Delta\alpha$ and a positive Δn in the case of the above-band-gap excitations, resulting in a positive ΔR . The free-carrier absorption mechanism, usually negligible compared to the two aforementioned mechanisms,^{31,32} contributes to a negative ΔR . While all of these mechanisms are simultaneously present, the observed negative ΔR suggests the dominant role of the band gap renormalization.

The decay of ΔR also involves many possible carrier relaxation and recombination processes. Here, we first present a possible scenario based on hot carrier relaxation (cooling) that accounts for the fast initial decay of ΔR ; we then discuss reasons for excluding other possible mechanisms. As mentioned above, the negative ΔR indicates a strong band gap renormalization effect. At zero time delay, the generated carriers have higher energies than the band gap, that is, they are hot carriers. As these hot carriers relax, most likely via optical phonon emissions, they begin to occupy the states close to the band edges, leading to a strong band-filling effect that becomes more significant over time.³⁴ As discussed above, the band-filling effect drives ΔR toward the positive direction, counteracting the band gap renormalization effect. The combined effect is the decay of $-\Delta R$. Therefore, the fast initial decay within a few picoseconds shown in Figure 2b represents the rising of the band-filling effect and thus the time scale of the hot carrier cooling. Comprehensive simulations of the ultrafast pump–probe reflectivity in semiconductors have also shown that the positive-going portion of ΔR represents the carrier cooling process.³⁴

We note that many other mechanisms can contribute to the fast initial decay of $-\Delta R$, such as carrier–carrier scattering, radiative recombination of the electron–hole plasma, Auger recombination, and carrier trapping. The time scale of the carrier–carrier scattering in highly excited semiconductors at room temperature is typically on the order of 10 fs,³⁵ beyond the time resolution of our studies. Moreover, carrier–carrier

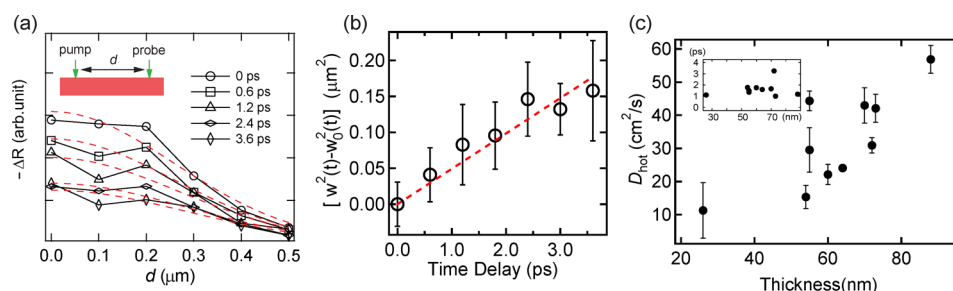


Figure 4. (a) $-\Delta R$ as a function of the distance, d , between pump and probe beams at specific delay times, with the dashed lines representing Gaussian fittings; (b) $[w(t)^2 - w_0(t)^2]$ as a function of delay time, with the dashed line as the linear fitting; (c) the dependence of the ambipolar hot carrier diffusion coefficient, D_{hot} , on the CuInSe_2 nanosheet thickness, with the hot carrier cooling time constant, τ , as a function of thickness shown in the inset.

scattering and radiative and Auger recombinations are expected to become more efficient (i.e., a faster $-\Delta R$ decay) with increasing generated carrier density,³⁶ which is opposite to our observations (Figures 3a–c; see also below). Indeed, at longer delay times, we observed the decays of $-\Delta R$ with characteristics indicating Auger or bimolecular carrier recombinations in these nanosheets (Supporting Information). Carrier trapping, on the other hand, would lead to a slower $-\Delta R$ decay with a larger carrier density due to the saturation of traps. However, carrier traps in CuInSe_2 have trapping times on the order of tens of microseconds to milliseconds.³⁷ Therefore, we attribute the fast initial decay of ΔR to the hot carrier cooling process.

As shown in Figure 2b, the hot carrier cooling process has a time scale of ~ 5 ps. For consistent measurements, we use an exponential fitting to extract the cooling time constant, τ , as shown in Figure 3a.³⁸ The fitting parameters for Figure 3a are included in the Supporting Information. We note that the exponential fitting in some cases yields τ smaller than the temporal resolution of our setup (0.6 ps); however, the hot carrier cooling process, the entire duration of which can be estimated from the peak of $-\Delta R$ to the constant background (e.g., the shaded region in Figure 2b), always persists longer than the instrument resolution, with the comparison shown in Figure 3c and the inset. For consistency, we use τ extracted from the exponential fittings as the characteristic time of the hot carrier cooling. For all of the CuInSe_2 nanosheets studied, τ was found to increase with the increasing pump fluence (i.e., carrier density). We have verified the robustness of this behavior by comparing τ measured during the ramp-up and the ramp-down of the pump fluence, and similar characteristics were observed. This increase in τ , that is, the decrease in hot carrier cooling rate, as the hot carrier density increases is consistent with the hot phonon bottleneck effect.^{39,40} This effect arises when large nonequilibrium optical phonon populations are generated by hot carrier cooling, and these hot phonons can be reabsorbed by hot carriers, impeding the cooling process of the hot carriers. The observation of this effect further validates the dominant role of the hot carrier cooling in the initial decay of $-\Delta R$.

Besides the cooling process, the diffusion of hot carriers is also an important aspect in hot carrier dynamics and is relevant to hot carrier solar cell operations. We note that because the densities of excited hot electrons and holes in our studies are large (10^{19} – 10^{20} cm^{-3}), the diffusion of the hot carriers is of ambipolar nature.⁴¹ To probe the hot carrier diffusion, we spatially separated pump and probe beams,^{42,43} as shown schematically in the inset to Figure 4a, and recorded $-\Delta R$ as a function of the distance (d) between pump and probe beams at

specific delay times. The measured $-\Delta R$ versus d relations, as shown in Figure 4a, can be used to obtain the hot carrier spatial profiles at specific delay times. The out-diffusion of hot carriers is expected to broaden the spatial profiles as a function of the time delay. By measuring this broadening, the diffusion coefficient of the hot carriers can be extracted. However, several factors need to be considered. First, the spatial profiles in Figure 4a are convoluted with the probe beam spatial profile, and a deconvolution procedure is necessary to extract the real spatial profiles of the hot carriers. In addition, the hot carrier out-diffusion is not the only mechanism that leads to the change in the spatial profile width. Specifically, because the cooling of the hot carriers is slower when the hot carrier density is higher, the number of the hot carriers decays slower in the center of the pump beam spot, where the hot carrier density is higher, than that in the regions away from the center. This mechanism alone would lead to a narrowing of the hot carrier spatial profile over time, and this effect needs to be included in extracting the diffusion coefficient. Details of the procedures that take into account these factors in obtaining the hot carrier spatial profiles are included in the Supporting Information.

After the deconvolution procedure and taking into account the narrowing effect of the hot carrier spatial profile over time, we determined $w(t)^2 - w_0(t)^2$, where $w(t)$ is the full-width-at-half-maximum (fwhm) of the experimentally measured hot carrier spatial profile at the delay time t and $w_0(t)$ is the fwhm of the calculated hot carrier spatial profile with the narrowing effect but without the carrier diffusion. $w_0(t)$ therefore represents the “baseline” for determining the spatial profile broadening (see the Supporting Information). Using the relation $w(t)^2 - w_0(t)^2 = 16 \ln(2) D_{\text{hot}} t$, where D_{hot} is the ambipolar hot carrier diffusion coefficient and t is the delay time,^{32,44} D_{hot} can be extracted from the linear fitting to the relation of $[w(t)^2 - w_0(t)^2]$ versus t , as shown in Figure 4b. We determined D_{hot} in CuInSe_2 nanosheets with various thicknesses, and the value of D_{hot} was found to increase from ~ 11 to $\sim 57 \text{ cm}^2/\text{s}$ as the nanosheet thickness increased from ~ 26 to $\sim 88 \text{ nm}$ (Figure 4c). To the best of our knowledge, this is the first measurement of D_{hot} in CuInSe_2 . The obtained values, while lower than those measured in graphene ($\sim 10^4 \text{ cm}^2/\text{s}$), are comparable to those determined at 80 K in bulk InP ($\sim 110 \text{ cm}^2/\text{s}$). It is also useful to compare D_{hot} to the diffusion coefficients of relaxed carriers (i.e., carriers in equilibrium with the lattice) in single-crystal CuInSe_2 , ~ 6 – $17 \text{ cm}^2/\text{s}$ for electrons and ~ 0.7 – $1 \text{ cm}^2/\text{s}$ for holes at 300 K.^{45–47} The higher value of D_{hot} can be accounted for by the higher kinetic energy of the hot carriers.

The dependence of D_{hot} on the nanosheet thickness, demonstrated in Figure 4c, indicates the size effects. Here, the CuInSe₂ nanosheet thickness is larger than the exciton Bohr radius (~ 11 nm) in CuInSe₂,⁴⁸ therefore effects of the quantum confinement of carriers can be excluded. In general, carrier–phonon and carrier–impurity scatterings are the major mobility-limiting mechanisms in bulk semiconductors. In nanoscale materials, carrier–phonon interactions can be modified by the quantum confinement of phonons, and the carrier–surface scattering might also play an important role. Here, the hot carrier cooling time constant (at the pump fluence of $\sim 287 \mu\text{J}/\text{cm}^2$), which is a measure of the strength of the carrier–phonon interaction, shows little variations with the CuInSe₂ nanosheet thickness (inset to Figure 4c). This suggests negligible changes to the carrier–phonon interaction strength. As all CuInSe₂ nanosheets were synthesized under the same conditions, significant variations of impurity concentrations are unlikely. On the other hand, carrier–surface scattering likely contributes to the thickness dependence of D_{hot} . Another possible mechanism is the scattering of carriers by the phonons in the SiO₂ substrate. This remote phonon scattering plays an important role in carrier dynamics in graphene.⁴⁹ Here, as the CuInSe₂ nanosheet thickness decreases, the interactions between carriers in the nanosheets and the remote phonons can be expected to become stronger, leading to a decrease in D_{hot} . Further experiments on suspended nanosheets might shed light on the significance of this mechanism.

In summary, we have synthesized single-crystal CuInSe₂ nanosheets and studied the ultrafast carrier dynamics and transport in this 2D material. In particular, results from femtosecond pump–probe optical reflectivity measurements suggest the dominant role of hot carrier cooling in carrier dynamics within a few picoseconds following the optical excitation. By studying the spatial profiles of hot carriers at various time intervals coupled to simple model calculations, we have obtained the ambipolar hot carrier diffusion coefficient and its dependence on CuInSe₂ nanosheet thickness. Possible mechanisms for such a dependence include carrier–surface and remote phonon scattering. These findings, for the first time, elucidate the hot carrier dynamics and transport properties in 2D single-crystal CuInSe₂ and provide practical guidance in exploring hot carrier effects in relevant nanoscale solar cells.

■ ASSOCIATED CONTENT

■ Supporting Information

Absorbance spectrum, calculations of the change to the optical reflectivity as a function of variations in the absorption coefficient and the real refractive index, long-time scans of $-\Delta R$, fitting parameters, procedures of the deconvolution, and the determination of the spatial profile width of the hot carrier in the absence of carrier diffusion. This material is available free of charge via the Internet at <http://pubs.acs.org>.

■ AUTHOR INFORMATION

Corresponding Author

*E-mail: yigu@wsu.edu.

Notes

The authors declare no competing financial interest.

■ ACKNOWLEDGMENTS

This work was partially supported by NSF (DMR-1206960). We thank Prof. Matt McCluskey and his group for the optical absorption measurements.

■ REFERENCES

- (1) Sze, S. M. *Physics of Semiconductor Devices*, 2nd ed.; Jon Wiley & Sons: New York, 1981.
- (2) Gorfinkel, V. B.; Luryi, S.; Gelmont, B. Theory of Gain Spectra for Quantum Cascade Lasers and Temperature Dependence of Their Characteristics at Low and Moderate Carrier Concentrations. *IEEE J. Quantum Electron.* **1996**, *32*, 1995–2003.
- (3) Ross, R. T.; Nozik, A. J. Efficiency of Hot-Carrier Solar-Energy Converters. *J. Appl. Phys.* **1982**, *53*, 3813–3818.
- (4) McGuire, J. A.; Joo, J.; Pietryga, J. M.; Schaller, R. D.; Klimov, V. I. New Aspects of Carrier Multiplication in Semiconductor Nanocrystals. *Acc. Chem. Res.* **2008**, *41*, 1810–1819.
- (5) Tisdale, W. A.; Williams, K. J.; Timp, B. A.; Norris, D. J.; Aydil, E. S.; Zhu, X. Y. Hot-Electron Transfer from Semiconductor Nanocrystals. *Science* **2010**, *328*, 1543–1547.
- (6) Nair, G.; Chang, L. Y.; Geyer, S. M.; Bawendi, M. G. Perspective on the Prospects of a Carrier Multiplication Nanocrystal Solar Cell. *Nano Lett.* **2011**, *11*, 2145–2151.
- (7) Pandey, A.; Guyot-Sionnest, P. Hot Electron Extraction from Colloidal Quantum Dots. *J. Phys. Chem. Lett.* **2010**, *1*, 45–47.
- (8) Kirk, A. P.; Fischetti, M. V. Fundamental Limitations of Hot-Carrier Solar Cells. *Phys. Rev. B* **2012**, *86*, 165206/1–165206/12.
- (9) Tielrooij, K. J.; Song, J. C. W.; Jensen, S. A.; Centeno, A.; Pesquera, A.; Elorza, A. Z.; Bonn, M.; Levitov, L. S.; Koppens, F. H. L. Photoexcitation Cascade and Multiple Hot-Carrier Generation in Graphene. *Nat. Phys.* **2013**, *9*, 248–252.
- (10) Nair, R. R.; Blake, P.; Grigorenko, A. N.; Novoselov, K. S.; Booth, T. J.; Stauber, T.; Peres, N. M. R.; Geim, A. K. Fine Structure Constant Defines Visual Transparency of Graphene. *Science* **2008**, *320*, 1308–1308.
- (11) Bernardi, M.; Palummo, M.; Grossman, J. C. Extraordinary Sunlight Absorption and One Nanometer Thick Photovoltaics Using Two-Dimensional Monolayer Materials. *Nano Lett.* **2013**, *13*, 3664–3670.
- (12) Ramasubramanian, A. Large Excitonic Effects in Monolayers of Molybdenum and Tungsten Dichalcogenides. *Phys. Rev. B* **2012**, *86*, 115409/1–115409/6.
- (13) Repins, I.; Contreras, M. A.; Egaas, B.; DeHart, C.; Scharf, J.; Perkins, C. L.; To, B.; Noufi, R. 19.9%-Efficient ZnO/CdS/CuInGaSe₂ Solar Cell with 81.2% Fill Factor. *Prog. Photovoltaics* **2008**, *16*, 235–239.
- (14) Chirila, A.; Buecheler, S.; Pianezzi, F.; Bloesch, P.; Gretener, C.; Uhl, A. R.; Fella, C.; Kranz, L.; Perrenoud, J.; Seyrling, S.; et al. Highly Efficient Cu(In,Ga)Se₂ Solar Cells Grown on Flexible Polymer Films. *Nat. Mater.* **2011**, *10*, 857–861.
- (15) Jeong, S.; Lee, B. S.; Ahn, S.; Yoon, K.; Seo, Y. H.; Choi, Y.; Ryu, B. H. An 8.2% Efficient Solution-Processed CuInSe₂ Solar Cell Based on Multiphase CuInSe₂ Nanoparticles. *Energ Environ. Sci.* **2012**, *5*, 7539–7542.
- (16) Kar, M.; Agrawal, R.; Hillhouse, H. W. Formation Pathway of CuInSe₂ Nanocrystals for Solar Cells. *J. Am. Chem. Soc.* **2011**, *133*, 17239–17247.
- (17) Reifsnnyder, D. C.; Ye, X. C.; Gordon, T. R.; Song, C. Y.; Murray, C. B. Three-Dimensional Self-Assembly of Chalcopyrite Copper Indium Diselenide Nanocrystals into Oriented Films. *ACS Nano* **2013**, *7*, 4307–4315.
- (18) Seo, Y. H.; Lee, B. S.; Jo, Y.; Kim, H. G.; Choi, Y.; Ahn, S.; Yoon, K.; Woo, K.; Moon, J.; Ryu, B. H.; et al. Facile Microwave-Assisted Synthesis of Multiphase CuInSe₂ Nanoparticles and Role of Secondary CuSe Phase on Photovoltaic Device Performance. *J. Phys. Chem. C* **2013**, *117*, 9529–9536.
- (19) Stolle, C. J.; Harvey, T. B.; Pernik, D. R.; Hibbert, J. I.; Du, J.; Rhee, D. J.; Akhavan, V. A.; Schaller, R. D.; Korgel, B. A. Multiexciton

Solar Cells of CuInSe₂ Nanocrystals. *J. Phys. Chem. Lett.* **2014**, *5*, 304–309.

(20) Panthani, M. G.; Stolle, C. J.; Reid, D. K.; Rhee, D. J.; Harvey, T. B.; Akhavan, V. A.; Yu, Y. X.; Korgel, B. A. CuInSe₂ Quantum Dot Solar Cells with High Open-Circuit Voltage. *J. Phys. Chem. Lett.* **2013**, *4*, 2030–2034.

(21) Schoen, D. T.; Peng, H. L.; Cui, Y. CuInSe₂ Nanowires from Facile Chemical Transformation of In₂Se₃ and Their Integration in Single-Nanowire Devices. *ACS Nano* **2013**, *7*, 3205–3211.

(22) Steinhagen, C.; Akhavan, V. A.; Goodfellow, B. W.; Panthani, M. G.; Harris, J. T.; Holmberg, V. C.; Korgel, B. A. Solution–Liquid–Solid Synthesis of CuInSe₂ Nanowires and Their Implementation in Photovoltaic Devices. *ACS Appl. Mater. Interface* **2011**, *3*, 1781–1785.

(23) Tao, X.; Gu, Y. Crystalline–Crystalline Phase Transformation in Two-Dimensional In₂Se₃ Thin Layers. *Nano Lett.* **2013**, *13*, 3501–3505.

(24) Jacobs-Gedrim, R. B.; Shanmugam, M.; Jain, N.; Durcan, C. A.; Murphy, M. T.; Murray, T. M.; Matyi, R. J.; Moore, R. L.; Yu, B. Extraordinary Photoresponse in Two-Dimensional In₂Se₃ Nanosheets. *ACS Nano* **2014**, *8*, 514–521.

(25) Hsin, C. L.; Lee, W. F.; Huang, C. T.; Huang, C. W.; Wu, W. W.; Chen, L. J. Growth of CuInSe₂ and In₂Se₃/CuInSe₂ Nano-Heterostructures through Solid State Reactions. *Nano Lett.* **2011**, *11*, 4348–4351.

(26) Tao, X.; Mafi, E.; Gu, Y. Ultrafast Carrier Dynamics in Single-Crystal In₂Se₃ Thin Layers. *Appl. Phys. Lett.* **2013**, *103*, 193115/1–193115/4.

(27) Schoen, D. T.; Peng, H. L.; Cui, Y. Anisotropy of Chemical Transformation from In₂Se₃ to CuInSe₂ Nanowires through Solid State Reaction. *J. Am. Chem. Soc.* **2009**, *131*, 7973–7975.

(28) Alvarez-Garcia, J.; Barcones, B.; Perez-Rodriguez, A.; Romano-Rodriguez, A.; Morante, J. R.; Janotti, A.; Wei, S. H.; Scheer, R. Vibrational and Crystalline Properties of Polymorphic CuInC₂ (C=Se,S) Chalcogenides. *Phys. Rev. B* **2005**, *71*, 054303/1–054303/9.

(29) Rincon, C.; Ramirez, F. J. Lattice-Vibrations of CuInSe₂ and CuGaSe₂ by Raman Microspectrometry. *J. Appl. Phys.* **1992**, *72*, 4321–4324.

(30) Vorlicek, V.; Zelezny, V.; Tiwari, A. N.; Krejci, M.; Zogg, H. Determination of the Crystallographic Orientation of CuInSe₂ Thin Films by Raman and Infrared Spectroscopy. *J. Appl. Phys.* **1997**, *82*, 5484–5487.

(31) Tang, Y.; Braunstein, R.; Vonroedern, B. Determination of Drift Mobility and Lifetime for Dominant Charge-Carriers in Polycrystalline CuInSe₂ by Photomixing. *Appl. Phys. Lett.* **1993**, *63*, 2393–2395.

(32) Wang, R.; Ruzicka, B. A.; Kumar, N.; Bellus, M. Z.; Chiu, H. Y.; Zhao, H. Ultrafast and Spatially Resolved Studies of Charge Carriers in Atomically Thin Molybdenum Disulfide. *Phys. Rev. B* **2012**, *86*, 045406/1–045406/5.

(33) Bennett, B. R.; Soref, R. A.; Delalano, J. A. Carrier-Induced Change in Refractive-Index of InP, GaAs, and InGaAsP. *IEEE J. Quantum Electron.* **1990**, *26*, 113–122.

(34) Prabhu, S. S.; Vengurlekar, A. S. Dynamics of the Pump–Probe Reflectivity Spectra in GaAs and GaN. *J. Appl. Phys.* **2004**, *95*, 7803–7812.

(35) Becker, P. C.; Fragnito, H. L.; Cruz, C. H. B.; Fork, R. L.; Cunningham, J. E.; Henry, J. E.; Shank, C. V. Femtosecond Photon-Echoes from Band-to-Band Transitions in GaAs. *Phys. Rev. Lett.* **1988**, *61*, 1647–1649.

(36) Kunneman, L. T.; Tessier, M. D.; Heuclin, H.; Dubertret, B.; Aulin, Y. V.; Grozema, F. C.; Schins, J. M.; Siebbeles, L. D. A. Bimolecular Auger Recombination of Electron–Hole Pairs in Two-Dimensional CdSe and CdSe/CdZnS Core/Shell Nanoplatelets. *J. Phys. Chem. Lett.* **2013**, *4*, 3574–3578.

(37) Tabibazar, M.; Möller, H. J.; Shoemaker, N. Trapping Lifetime and Carrier Mobility Measurements in CuInSe₂ Using Surface-Acoustic-Wave Technique. *IEEE T Ultrason. Ferroelectrics* **1993**, *40*, 149–153.

(38) The scans were shifted by –0.4 ps, so that the –ΔR signal from the nanosheets started from time zero.

(39) Lugli, P.; Goodnick, S. M. Nonequilibrium Longitudinal-Optical Phonon Effects in GaAs–AlGaAs Quantum-Wells. *Phys. Rev. Lett.* **1987**, *59*, 716–719.

(40) Nozik, A. J. Spectroscopy and Hot Electron Relaxation Dynamics in Semiconductor Quantum Wells and Quantum Dots. *Annu. Rev. Phys. Chem.* **2001**, *52*, 193–231.

(41) In semiconductors, electrons usually have larger mobilities and diffusion constants than holes. However, when the densities of the photogenerated electrons and holes are quite high, such as in our case, electrons and holes move together due to strong Coulomb interactions between them. As a result, electrons and holes have the same mobility and diffusion constant, in which case the diffusion is ambipolar in nature.

(42) Gabriel, M. M.; Kirschbrown, J. R.; Christesen, J. D.; Pinion, C. W.; Zigler, D. F.; Grumstrup, E. M.; Mehl, B. P.; Cating, E. E. M.; Cahoon, J. F.; Papanikolas, J. M. Direct Imaging of Free Carrier and Trap Carrier Motion in Silicon Nanowires by Spatially-Separated Femtosecond Pump–Probe Microscopy. *Nano Lett.* **2013**, *13*, 1336–1340.

(43) Lo, S. S.; Shi, H. Y.; Huang, L. B.; Hartland, G. V. Imaging the Extent of Plasmon Excitation in Au Nanowires Using Pump–Probe Microscopy. *Opt. Lett.* **2013**, *38*, 1265–1267.

(44) Smith, L. M.; Wake, D. R.; Wolfe, J. P.; Levi, D.; Klein, M. V.; Klem, J.; Henderson, T.; Morkoc, H. Picosecond Imaging of Photoexcited Carriers in Quantum Wells — Anomalous Lateral Confinement at High-Densities. *Phys. Rev. B* **1988**, *38*, 5788–5791.

(45) Gorley, P. M.; Khomyak, V. V.; Vorobiev, Y. V.; Gonzalez-Hernandez, J. D.; Horley, P. P.; Galochkina, O. O. Electron Properties of N- and P-CuInSe₂. *Sol. Energy* **2008**, *82*, 100–105.

(46) Wasim, S. M.; Noguera, A. Transport-Properties of N-Type CuInSe₂. *Phys. Status Solidi A* **1984**, *82*, 553–559.

(47) Irie, T.; Endo, S.; Kimura, S. Electrical Properties of P- and N-Type CuInSe₂ Single Crystals. *Jpn. J. Appl. Phys.* **1979**, *18*, 1303–1310.

(48) Zhong, H. Z.; Wang, Z. B.; Bovero, E.; Lu, Z. H.; van Veggel, F. C. J. M.; Scholes, G. D. Colloidal CuInSe₂ Nanocrystals in the Quantum Confinement Regime: Synthesis, Optical Properties, and Electroluminescence. *J. Phys. Chem. C* **2011**, *115*, 12396–12402.

(49) Fratini, S.; Guinea, F. Substrate-Limited Electron Dynamics in Graphene. *Phys. Rev. B* **2008**, *77*, 195415/1–195415/6.